Nanoscale

PAPER

View Article Online
View Journal

Cite this: DOI: 10.1039/d5nr05011a

Random sequence-guided crosslinking for on-demand injectable HA–DNA hydrogels supporting neural progenitor cells

Taehyun Kim,†[a,b] Eunseo Han,†[a] Siyeon Park[a] and Jieung Baek *[a,b]

Received 27th November 2025,
Accepted 23rd March 2026

DOI: 10.1039/d5nr05011a

rsc.li/nanoscale

Hyaluronic acid (HA) hydrogels crosslinked through DNA hybridization (HA–DNA hydrogels) offer a programmable and cell-compatible platform for regenerative medicine. However, their practical use has been limited by undesired premature network formation arising from nonspecific hybridization among tethered strands. Here, we introduce an on-demand injectable HA–DNA hydrogel engineered through a dual-tube hybrid-bridge design coupled with sequence-level randomization to regulate gelation kinetics. Randomization was expected to disrupt excessive complementarity among identical crosslinkers, reducing nonspecific self-dimerization. Each HA chain was conjugated with an anchor DNA strand and pre-hybridized with a one crosslinker type (Tube A or Tube B), after which the two solutions were mixed to trigger on-demand gelation. *In silico* analysis identified that introducing randomized bases into the crosslinker overlap domain, with a total randomized length of $N = 8$, minimized undesired self-dimerization while preserving productive hybridization. Consistently, rheological analyses confirmed these predictions, showing suppressed pre-gelation in single-tube condition and rapid, homogeneous gelation upon precursor mixing. Furthermore, the optimized $N = 8$ hydrogel enabled uniform encapsulation of neural progenitor cells, supporting high viability and sustained expression of neural stemness-associated markers (*SOX2*, *NESTIN*). Above all, the hydrogel further exhibited injectable capability with shear-thinning, rapid self-healing, and robust post-extrusion structural integrity, enabling minimally invasive delivery without compromising cell proliferation. Collectively, this sequence-optimized dual-tube strategy establishes a versatile and programmable HA–DNA hydrogel platform for controlled gelation and injectable neural tissue engineering applications.

Introduction

Hyaluronic acid (HA) has been extensively utilized to develop biocompatible and injectable hydrogel scaffolds for cell delivery and tissue regeneration.[1–5] In particular, HA-based hydrogels have been widely applied in neural tissue engineering because they provide an extracellular matrix (ECM)-mimicking microenvironment as a major component of brain ECM, supporting neural stem cell survival, differentiation, and axonal regeneration.[5–9] As a crosslinking strategy for HA-based hydrogels, DNA hybridization offers a programmable mechanism for reversible crosslinking under mild physiological conditions, enabling fine control over network formation.[10–13] However, despite these advantages, current HA hydrogels with DNA hybridization-based crosslinking (HA–DNA gel) systems still encounter challenges in regulating gelation kinetics because of the intrinsic property of nonspecific or premature hybridization between tethered DNA strands within concentrated HA chains.[14,15] Such spontaneous association often triggers undesired pre-gel aggregation, reducing injectability and reproducibility during hydrogel fabrication.[16–18] To address this issue, strategies for precise temporal and spatial control over DNA-mediated gelation while maintaining structural homogeneity and functional responsiveness have been reported to facilitate the translation of these HA–DNA hydrogels into practical biomedical applications.[12–15]

The simplest strategy for constructing HA–DNA hydrogels involves grafting two HA chains with complementary DNA anchor strands that hybridize directly upon mixing, forming physical crosslinks through base-pair hybridization.[19,20] This complementary anchor design leads to rapid network formation through spontaneous base pairing between the two anchor strands. However, this direct hybridization is inherently difficult to control, as strand pairing begins immediately upon contact, leading to premature aggregation that compromises the injectability and structural uniformity of the hydro-

---

[a] *Department of Mechanical and Biomedical Engineering, Ewha Womans University, Seoul, 03760, Republic of Korea. E-mail: jieungbaek@ewha.ac.kr*
[b] *Graduate Program in System Health Science and Engineering, Ewha Womans University, Seoul, 03760, Republic of Korea*

† These authors contributed equally to this work.

gel network.[18,21] Consequently, uncontrolled solidification during mixing or injection often restricts uniform dispersion and reduces the reproducibility of hydrogel formation. These limitations make it difficult to maintain a stable sol state before delivery and to achieve on-demand gelation at the target site, both of which are essential prerequisites for injectable hydrogel applications.[22,23]

To delay gelation and achieve better control over network formation, a "bridge-mediated" strategy was developed, in which a separate bridge oligonucleotide connects two distinct HA–DNA anchor strands, providing indirect crosslinking that allows fine regulation of hybridization kinetics and gelation behavior.[20,24,25] This indirect hybridization further enables modulation of crosslinking density through adjustments in bridge sequence and length, offering a higher degree of structural programmability compared with the direct pairing approach. However, in practice, the bridge strand often still exhibits unintended partial hybridization with a single anchor before interacting with its complementary counterpart, leading to local pre-network formation and a gradual increase in solution viscosity even before fully mixing.[10,25] Consequently, premature gelation can still occur, undermining injectability and reproducibility, and this emphasizes the need for more precise strategies to temporally regulate DNA-mediated gelation.

Here, we developed a dual-solution, preloaded hybrid-bridge strategy designed to temporally regulate DNA-mediated crosslinking. In this system, each HA chain was conjugated with an anchor DNA strand and pre-hybridized with one of two distinct bridge oligonucleotides, generating two independent precursor solutions (designated as Tube A and Tube B) (Fig. 1). Because the bridge was only partially hybridized, both solutions were expected to remain fluid and stable, avoiding nonspecific network formation before mixing. Nevertheless, even under this two-tube configuration, undesired assemblies such as anchor–anchor pairing and crosslinker self-hybridization were occasionally observed, leading to partial pre-gelation. To further suppress these side interactions, we added randomized sequence domains within the bridge strands, motivated by a recent finding that randomization restricts excessive undesired hybridization.[26] We performed *in silico* hybridization analysis using the Nucleic Acid Package (NUPACK) algorithm to calculate the degree of undesired assemblies, systematically varying the number of randomized bases (N) within the bridge sequence. Among the randomized domain lengths tested (N = 0, 4, 8, and 10), N = 8 and N = 10 exhibited a reduced propensity for undesired assembly while preserving higher productive hybridization for crosslinking, compared with the non-randomized condition (N = 0). Consistent with this, rheological analysis revealed that the condition with N = 8 yields rapid yet homogeneous network formation upon mixing with limited unintended pre-gelation before mixing. Furthermore, this HA–DNA hydrogel caused no significant damage to the cell viability of neural progenitor cells, maintaining the stemness marker expression level until 5 days above the original level before encapsulation. Furthermore, this hybridization mechanics allowed for effective injectability, exhibiting clear shear thinning and self-healing behaviors from rheology analysis. In particular, the cells maintained their viability and proliferative status after a syringe-mediated injection, demonstrating the potential of our HA–DNA gels with a randomized domain for injectable supporting materials. This dual-bridge system, combined with randomization, may offer precise temporal control over gelation and improve reproducibility for cell encapsulation and tissue-engineering applications. More broadly, this framework establishes a versatile and scalable hydrogel platform poised for minimally invasive delivery, regenerative therapies, and the rational engineering of next-generation programmable biomaterials.

Jieung Baek

Dr Jieung Baek is an Assistant Professor in the Department of Mechanical and Biomedical Engineering at Ewha Womans University. She received her Ph.D. in Chemical and Biomolecular Engineering from KAIST and completed postdoctoral training in Bioengineering at UC Berkeley. Her research integrates mechanobiology, nucleic acid (DNA) engineering, and 3D biomaterials to develop molecular screening platforms and mechanically tuned systems for precision control of cells and tissues, with applications in diagnostics, regenerative medicine, and disease reversal.

Results

Synthesis of methacrylated hyaluronic acid (HA-Me) and its conjugation with DNA anchor strands

To harness the DNA hybridization machinery for HA crosslinking, we first synthesized methacrylated hyaluronic acid (HA-Me) by reacting HA with methacrylic anhydride (MA) under alkaline conditions.[3,5,27,28] According to ^{1}H-NMR spectra, bare HA exhibited a characteristic N-acetyl methyl resonance at ~1.9 ppm, whereas HA-Me displayed additional methacrylate vinyl proton signals at ~5.2 and ~5.5 ppm and a distinct methacrylate methyl peak at ~1.8 ppm, which was well resolved from the HA methyl resonance (Fig. 2a).[29] The degree of methacrylation (DoM) was determined using the integrated intensities of these resolved peaks, and it was calculated as approximately 0.667 (≈66.7%). This substitution level indicates ~0.67 reactive methacrylates per repeat unit, which is sufficient to provide abundant coupling sites for DNA anchor strands while maintaining HA processability. Collectively, the spectrum substantiates efficient and tailorable methacrylation at a sufficiently high density for downstream thiol–Michael conjugation of anchor DNA.[30–32]

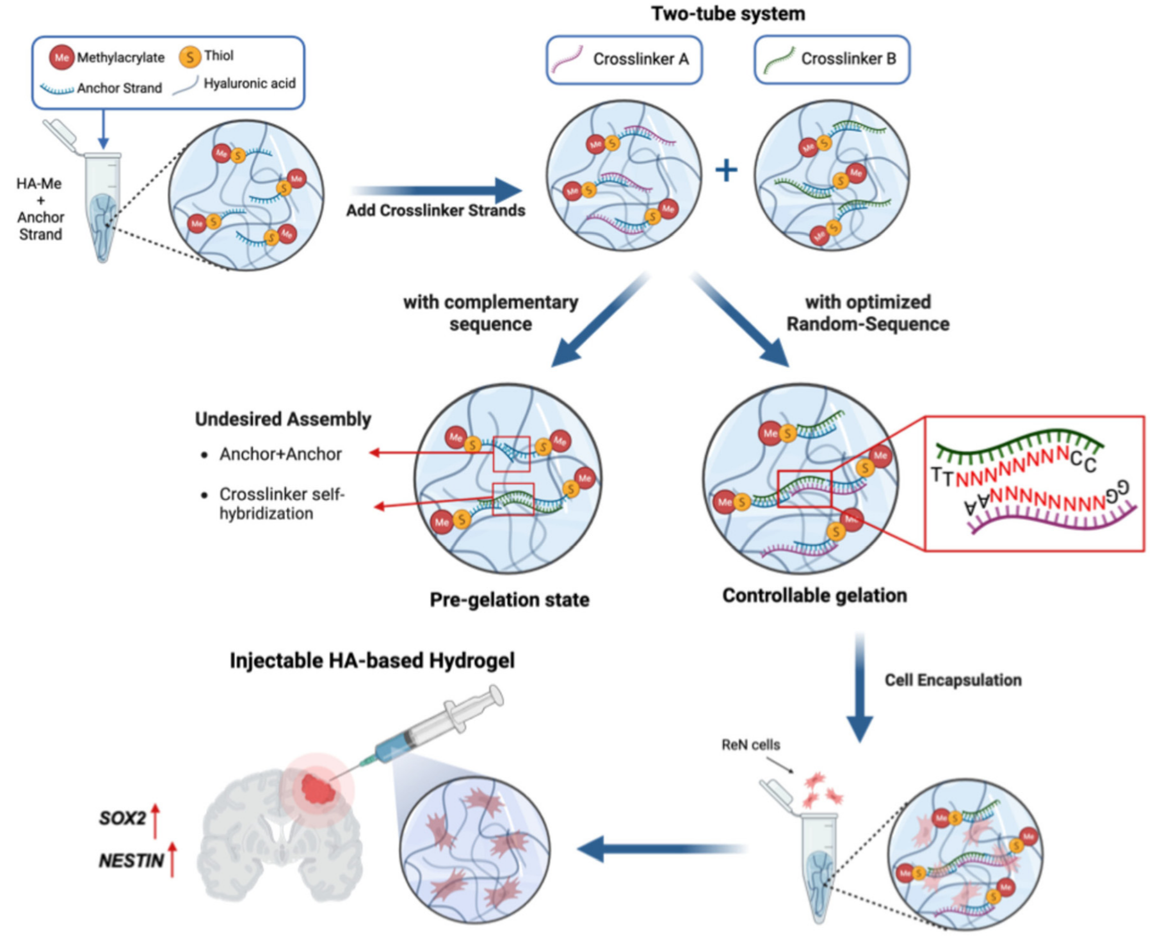

Fig. 1 Schematic illustration of on-demand injectable HA–DNA hydrogel gelation using a dual-tube system with randomized sequences. (Top) HA was modified with methacrylate (Me) and thiol (S) groups and conjugated with identical DNA anchor strands to form HA-Me-anchor precursors. (Middle) Incorporation of randomized overlap domains within the crosslinkers minimized non-productive hybridization and enabled on-demand gelation upon mixing. (Bottom) The optimized injectable HA-based hydrogel's potential as a biomimetic platform for neural tissue engineering.

We next validated the reactivity of the thiol moiety at the end of the DNA anchor strands, intended for subsequent Michael reaction-based conjugation to HA-Me, by using Ellman's assay.[33,34] After reduction of the anchor strands with dithiothreitol (DTT), the absorbance at 412 nm (A_{412}) was measured to detect free thiol groups and compared with two controls: a cysteine-containing peptide as a positive control and distilled water as a negative control (Fig. 2b). Both the reduced 5′-thiol anchor strand and the cysteine-containing peptide exhibited a pronounced increase in A_{412} compared with negative control. This increase corresponds to the formation of 2-nitro-5-thiobenzoate (TNB^-) upon reaction between free thiols and DTNB, confirming the successful reduction and exposure of reactive sulfhydryl groups on the anchor DNA.

Next, we evaluated covalent coupling between the HA-Me and the anchor strand by electrophoresis with two controls: only HA-Me without the anchor strand and the free anchor strand (Fig. 2c). The free anchor strand migrated as an expected ~22 bp band, whereas both HA-Me and HA-Me–anchor conjugates remained in the loading wells without any visible band at ~22 bp. If a substantial amount of anchor strands had remained unbound to HA-Me, a band at ~22 bp would have also appeared in the conjugated sample. Therefore, the absence of such a band suggests efficient coupling of the DNA anchor strands to the HA-Me backbone.

Together, these results demonstrate that HA methacrylation and subsequent thiol-anchored DNA conjugation were achieved, yielding a functionalized HA matrix competent for downstream crosslinking based on DNA hybridization.

Optimization of random-domain length (*N*) for selective DNA hybridization

Spontaneous hybridization among partially complementary strands can lead to premature gelation even before complete mixing. These undesired assemblies, including anchor–anchor pairing, crosslinker self-hybridization, and intramolecular hybridization, would compromise the uniformity and reproducibility of hydrogel formation with loss of injectability. Although gelation could, in principle, be triggered by adding a

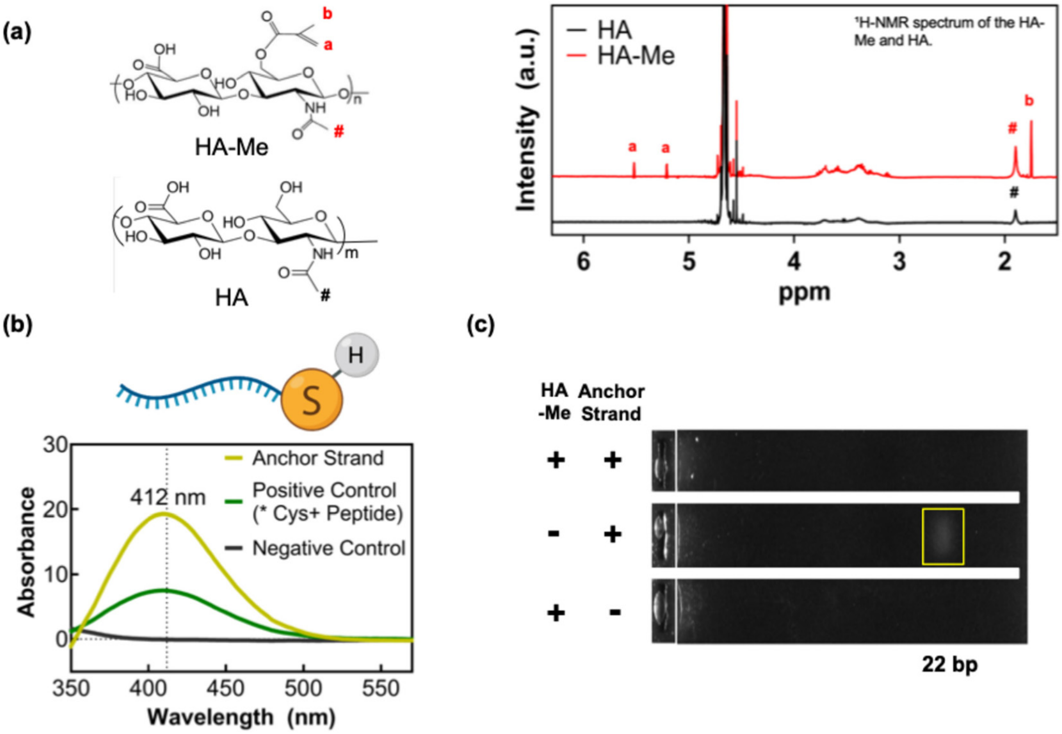

Fig. 2 Validation of HA methacrylation and anchor strand conjugation. (a) Chemical structures of HA-Me and bare HA, with ^{1}H assignments labeled (a = vinyl, b = methyl, # = *N*-acetyl-CH_3) and their ^{1}H-NMR spectra (D_2O): HA-Me (red) and HA (black). (b) Top: Schematic illustration of the thiol-modified anchor DNA; bottom: Ellman's assay (A_{412}) confirming the presence of free thiols after DTT reduction (positive control = Cys-peptide; negative control = no thiol). (c) Agarose gel electrophoresis showing that the free anchor strand migrates at ~22 bp, whereas HA-Me and the HA-Me-anchor conjugates remain in the loading wells.

single multivalent crosslinker to HA–anchor precursors, such one-shot approaches are inherently prone to crosslinker self-association and spatially heterogeneous gelation under practical mixing conditions. To overcome these limitations, we designed a dual-tube preloaded system in which each HA–anchor precursor was pre-hybridized with only one type of crosslinker (A or B).[35]

To further enhance the specificity of intermolecular hybridization only after mixing, we incorporated randomized bases into the overlap region of the crosslinkers to disrupt unwanted self-hybridization while maintaining productive complementary binding. Two crosslinker strands (A and B) were therefore synthesized, each containing a 22-base adaptor domain complementary to the HA-Me-anchored strand and a 14-base overlap region in which the number of randomized bases (N = 0, 4, 8, or 10) was systematically varied (Fig. 3a). The full nucleotide sequences of the anchor and crosslinker strands used in this study are provided in SI Table S1. We hypothesized that introducing partial randomness within the overlap domain would thermodynamically destabilize perfect self-hybridization of identical strands (anchor–anchor or crosslinker–crosslinker) by reducing local complementarity. In contrast, hybridization between complementary crosslinkers (A and B) was expected to remain energetically favorable, as the complementary pairing framework between the two strands was preserved despite the introduction of randomized nucleotides. This design was therefore intended to statistically weaken undesired self-interactions while maintaining productive hybridization required for network formation.[36,37]

Each crosslinker strand was pre-hybridized with its corresponding HA-Me–anchor to form two independent precursor solutions (Tube A and Tube B), constituting the dual-tube preloaded system (Fig. 3b). This configuration ensured that only one side of each bridge strand was initially hybridized, allowing both precursors to remain in a solution state before mixing.

To systematically evaluate how the random-domain length (N) affects hybridization specificity, we performed *in silico* equilibrium simulations using NUPACK. Because the N positions correspond to degenerate nucleotides introduced during oligonucleotides synthesis, the overlap region constitutes a sequence ensemble rather than a single defined strand. To model this ensemble system, all possible sequence combinations corresponding to the randomized positions (4^n variants; n = the number of N) were computationally enumerated for $N \leq 8$. For the $N = 10$ condition, the total number of possible sequence variants is substantially larger, therefore, 100 000 sequence variants were randomly sampled from the full combinatorial space. For each sequence variant, equilibrium complex concentration was calculated under identical

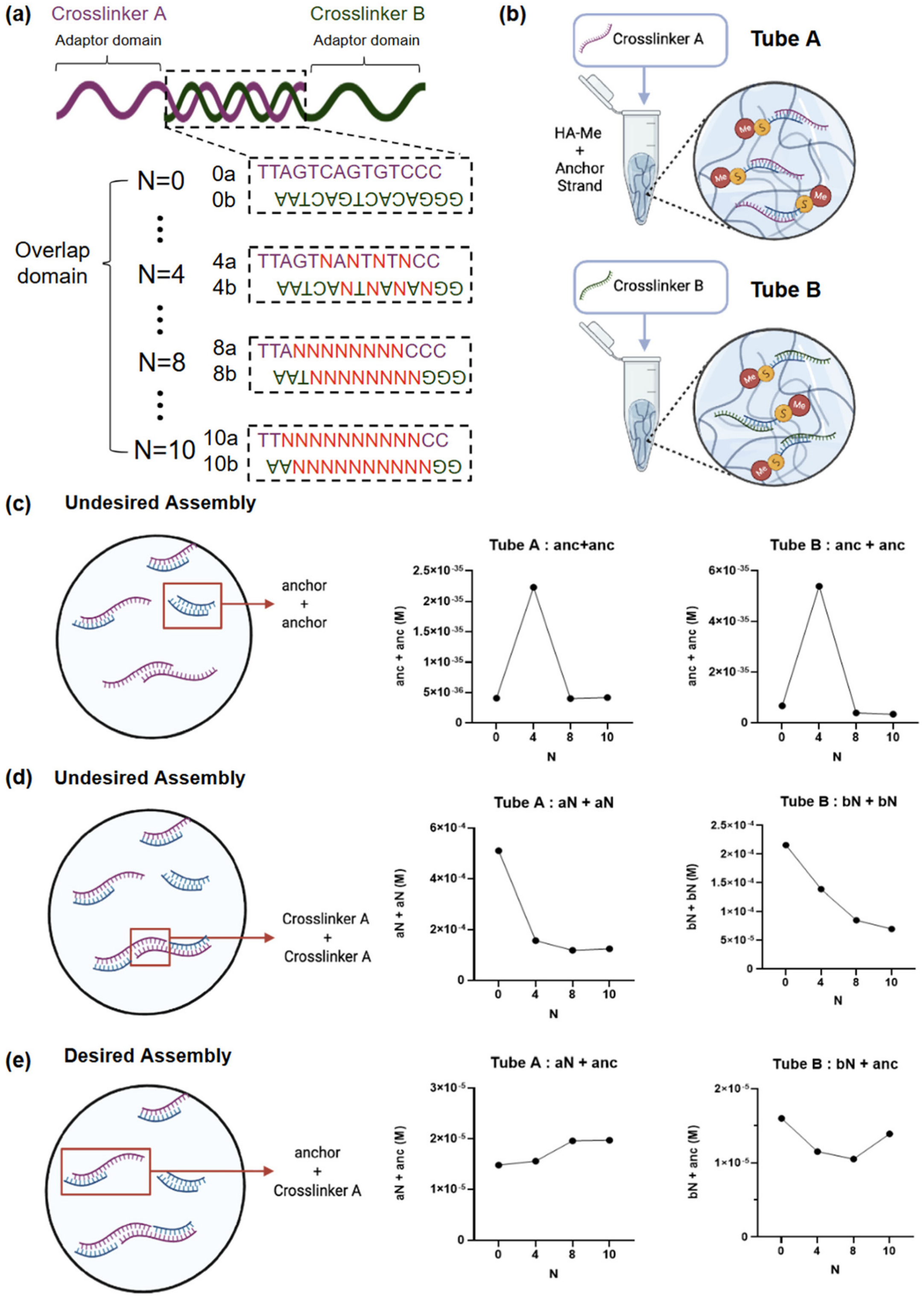

Fig. 3 *In silico* optimization of the random sequence domain (*N*) to prevent undesired assemblies. (a) Schematic design of the two complementary crosslinker strands (A and B). (b) Configuration of the two pre-gelation precursor tubes used for *in silico* analysis. Each tube represents the actual pre-mixing condition before final gelation. (c and d) NUPACK-predicted equilibrium complex concentrations illustrating the suppression of undesired self-assemblies with increasing random-domain length under physiological simulation conditions (37 °C; anchor 22.8 μM; crosslinker library 1150 μM): (c) anchor–anchor and (d) crosslinker–crosslinker misassemblies. (e) Equilibrium complex concentrations of productive anchor–crosslinker hybridization (*aN* + anc or *bN* + anc), obtained from ensemble-averaged simulations of all possible 4^n sequence variants.

thermodynamic conditions (37 °C, anc: 22.8 μM, crosslinker: 1150 μM). Ensemble-averaged values were then obtained to represent the overall hybridization behavior within each tube (Tube A: anchor + crosslinker A; Tube B: anchor + crosslinker B), with *N* varied from 0 to 10. In addition, all non-random regions involved in hybridization were designed to be fully complementary. Notably, one of the undesired self-dimerizations between anchor strands (anc + anc) exhibited overall negligible fractions but exhibited a distinctive dependency on the number of random bases for both tubes: with a transient increase at $N = 4$ followed by a decrease at $N = 8$ and 10 (Fig. 3c). This suggests that longer random domains effectively disrupt undesired self-hybridization. Dependency on the *N* was also observed for undesired crosslinker–crosslinker assemblies: crosslinker A (*aN*) + crosslinker A (*aN*) or crosslinker B (*bN*) + crosslinker B (*bN*) (Fig. 3d). The equilibrium concentration of these self-dimers decreased markedly with increasing *N*, indicating that sequence randomization effectively reduces self-complementarity-driven dimerization. In Tube A, the *aN* + *aN* concentration dropped sharply between $N = 0$ and 4 and then reached a plateau at minimal levels, whereas in Tube B, the *bN* + *bN* assemblies exhibited a more gradual yet continuous decrease across the entire *N* range. This difference likely reflects statistical differences in sequence ensemble behavior between the two crosslinker designs, although both followed the same overall trend of reduced self-hybridization with increasing *N*. On the other hand, the formation of desired anchor–crosslinker heterodimers (*aN* + anc or *bN* + anc) was maintained or slightly improved as *N* increased, particularly in Tube A (Fig. 3e). Altogether, incorporation of sufficiently long random domains ($N \geq 8$) statistically reduced undesired assemblies by increasing sequence heterogeneity and lowering the probability of fortuitous self-complementary interactions, while preserving productive hybridization required for network formation. In particular, $N = 8$ and 10 provided a balanced trade-off between minimized misassembly and stable target hybridization.

Rheological analysis with varying random-domain length (*N*)

Next, we performed rheological analysis to examine whether the simulated suppression of undesired assemblies translated into experimentally stable pre-gel conditions. Time- and frequency-sweep tests of single-crosslinker systems (Tube A or B) were first conducted to evaluate undesired spontaneous network formation before dual-crosslinking by mixing Tube A and B.

In the time-sweep test under constant strain (0.5%) and frequency (6 rad s^{-1}), samples with short or no random domains ($N = 0$ or 4) exhibited consistently higher storage moduli (G') than the loss moduli (G''), indicating undesired gel-like behavior likely driven by non-specific hybridization between partially complementary strands (Fig. 4a). In contrast, the $N = 8$ variant showed markedly fluid-like response ($G' \ll G''$) with large temporal fluctuations, demonstrating effective suppression of undesired associations and maintenance of a non-gelling pre-gel state. At $N = 10$, G' and G'' became comparable, indicating the formation of a weak, loosely crosslinked network. In the frequency sweep test (0.1–10 rad s^{-1}) under a constant strain of 0.5%, the viscoelastic profiles exhibited a clear dependence on the number of randomized bases (*N*) (Fig. 4b). Samples with $N = 0$, 4, and 10 showed frequency-independent, solid-like behavior ($G' > G''$), indicative of premature network formation. In contrast, the $N = 8$ variant showed a viscous-dominant profile ($G'' > G'$) across the frequency range from 0.1 rad s^{-1} to 10 rad s^{-1}.

These results are largely consistent with the previous NUPACK-based thermodynamic calculation in which Tube A with $N = 0$ or $N = 4$ exhibited relatively higher probabilities of undesired assembly than $N = 8$. In contrast to the equilibrium predictions, which suggested reduced self-dimerization at $N = 10$, rheological measurements revealed residual pre-gelation behavior similar to that observed for $N = 0$ and 4. This discrepancy suggests that excessive randomization, like $N = 10$, may increase the likelihood of partial or mismatched hybridization between unintended strands.

To further investigate this possibility, we additionally calculated the $\Delta G°$ values for potential undesired intermolecular hybridization (Fig. S1). Thermodynamic analyses of crosslinker self-association revealed that $N = 10$ variants exhibited more negative $\Delta G°$ values compared to $N = 8$, indicating a higher thermodynamic stability of unintended strand interactions. Such premature strand association can reduce the availability of reactive crosslinkers for intermolecular network formation and thus promote pre-gelation. These results suggest that while increasing the random domain length can reduce sequence matching errors, excessive sequence heterogeneity may increase the risk of undesired self-association.

Taken together, $N = 8$ provided the most balanced hybridization behavior with sufficient randomization to prevent undesired associations. Based on these results, $N = 8$ was selected as the optimal random-domain length for the next analysis.

To further validate this optimized condition, we also conducted rheological analysis on the Tube B system containing a single complementary crosslinker, with $N = 0$ and 8 (Fig. 4c). Both the time sweep and frequency sweep showed consistent suppression of spontaneous gelation and lower viscoelastic moduli in the Tube B with $N = 8$, compared to $N = 0$. Having confirmed that the optimized random-domain design ($N = 8$) consistently stabilizes both single-crosslinker systems (Tube A and B), we next examined whether this configuration enables well-controlled gelation upon mixing the two tubes (Fig. 4d). As a result, both the time and frequency sweeps showed G' higher than G'', indicating controlled gelation driven by crosslinker hybridization. Collectively, these results demonstrate that sequence-level randomization with $N = 8$ achieves precise temporal control over gelation, effectively resolving the trade-off between injectability and premature solidification in HA–DNA hydrogels. In addition, viscosity measurements of the individual precursor solutions (Tube A and Tube B, $N = 8$) further confirmed clear shear-thinning behavior with low apparent viscosity at increasing shear rates, supporting sufficient fluidity for homogeneous mixing prior to final gelation (Fig. S2).

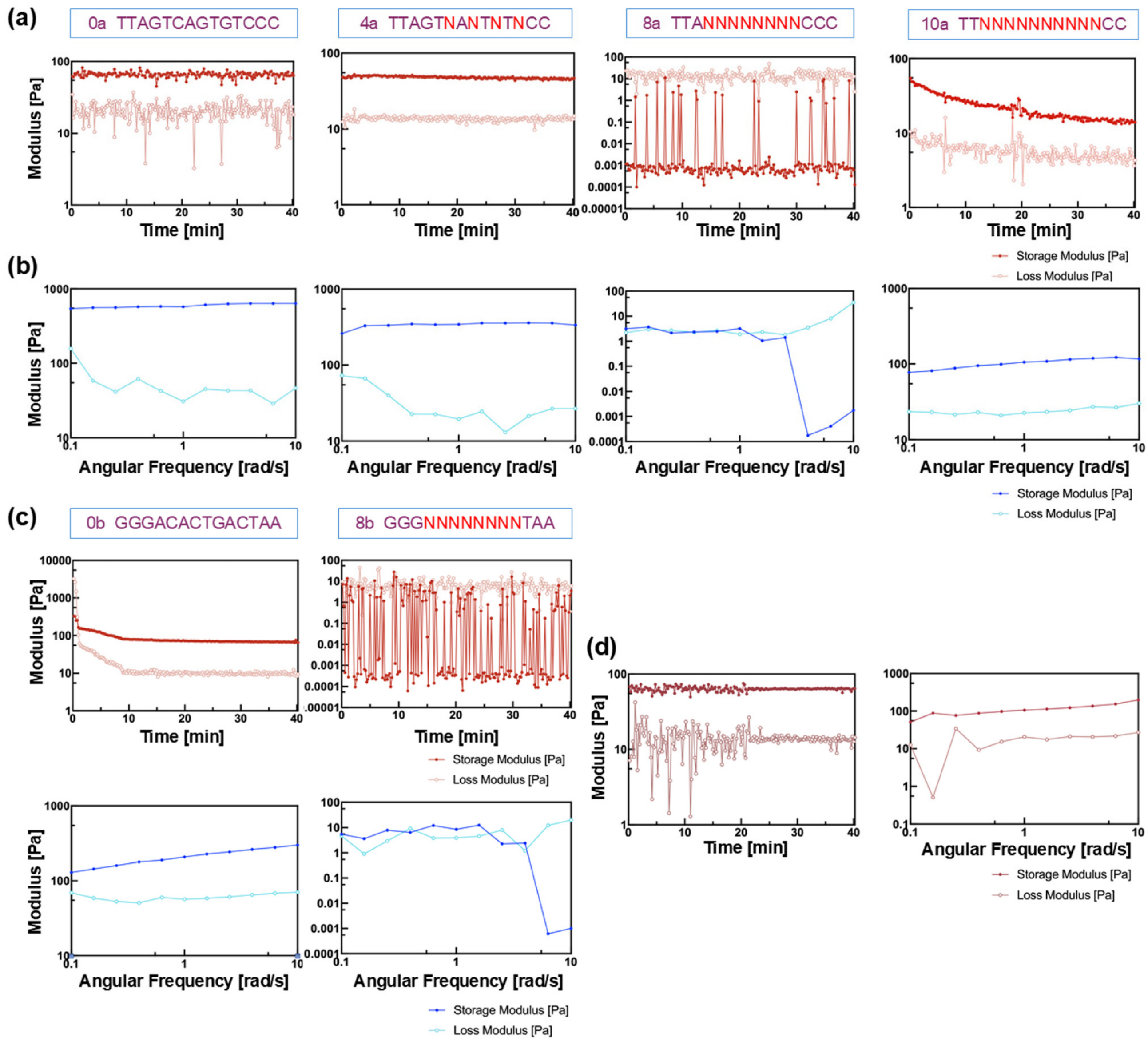

Fig. 4 Rheological analysis of anchor–crosslinker systems with varying random-domain length (*N*). (a) Time-sweep tests of single-crosslinker systems (Tube A) under constant strain (0.5%) and frequency (6 rad s^{-1}). (b) Frequency-sweep tests (0.1–10 rad s^{-1}) of Tube A under 0.5% strain. Rheological profiles (time and frequency sweep tests) of (c) Tube B and (d) the gels after dual-tube mixing (Tube A + Tube B) under the optimized *N* = 8 condition.

Characterization of neural progenitor cells encapsulated in HA–DNA hydrogel (*N* = 8)

Based on the results of NUPACK simulation and rheological analysis, the optimized *N* = 8 condition exhibited markedly restricted pre-gelation in the separate tube conditions (A and B), whereas the *N* = 0 solution showed clear pre-gelation behavior. To investigate whether such restricted pre-gelation enhances cell survival after encapsulation, we performed live/dead assays on ReN cells, a human neural progenitor cell line, using crosslinkers with *N* = 8 *versus* *N* = 0. In all the encapsulation conditions, cysteine-containing RGD peptide (Ac-GCGYGRGDSPG-NH_2) was incorporated into the HA–DNA hydrogel by thiol–Michael reaction to promote integrin-mediated cell engagement (Fig. 5a). As a result, both the *N* = 0 and *N* = 8 conditions supported cell survival, with over 90% cell viability (Fig. 5b and c). However, the number of live cells encapsulated within the gels was significantly higher in the *N* = 8 condition than in the *N* = 0 condition (Fig. 5d). Representative images from multiple randomly selected regions further confirmed the consistently lower cell density in the *N* = 0 gels (Fig. S3). In the *N* = 0 condition, premature gelation within each precursor tube increased viscosity prior to complete mixing, thereby limiting homogeneous cell incorporation. This demonstrates that pre-gelation driven by undesired assembly results in a marked reduction in cell encapsulation efficiency. Such restriction of premature network formation in the $N = 8$ condition may prevent an increase in local stiffness, enabling homogeneous cell dispersion during mixing and thereby allowing more cells to be incorporated into the final gel.

Following this validation of the $N = 8$ condition's cell entrapment yield and viability, we next monitored survival of the neural progenitor cells in the HA–DNA hydrogel ($N = 8$) over a period of 5 days (Fig. 5e). The encapsulated cells did not exhibit a significant decrease in cell viability over time, with most cells remaining Calcein AM-positive. Furthermore, ReN cells gradually formed multicellular spheroids within the $N = 8$ hydrogel over time. Time-course imaging from 0 h to 24 h further illustrated the progressive aggregation and compaction of cells into spheroid structures (Fig. S4). Such spheroid formation indirectly suggests that the optimized gel provides a sufficiently permissive and low-stress microenvironment that allows cell mobility, cell–cell aggregation, and maintenance of progenitor-like behavior.[9,38]

Next, we sought to examine the maintenance of neural stemness within the gel with a randomized domain ($N = 8$). The mRNA expression of neural stem cell markers *SOX2* and *NESTIN* was analyzed by qPCR (Fig. 5f).[38,39] Both markers were remarkably elevated at day 3 relative to day 0. Although they decreased by day 5, their levels remained higher than at day 0. These results indicate that the $N = 8$ gel serves as a microenvironmental cue that enhances or maintains the stemness of neural progenitor cells. The decline from day 3 to day 5 is assumed to result from apoptosis induced by hypoxia in the inner region of the neurosphere over time,[40] or from the onset of partial differentiation leading to a slight loss of stemness.[40] Overall, these results demonstrate that the HA–DNA hydrogel crosslinked with $N = 8$ effectively encapsulates neural progenitor cells, supports spheroid formation, and maintains stemness and viability.

Evaluating the injectability of HA–DNA hydrogel

Next, we assessed the injectability of HA–DNA hydrogel ($N = 8$) using rheological measurements and extrusion tests. Viscosity of the HA–DNA hydrogel was measured across different shear rates (0.1–100 s^{-1}) and found to decrease as the shear rates increased (Fig. 6a). This supports shear thinning behavior of the hydrogel, which is advantageous for injectability as it

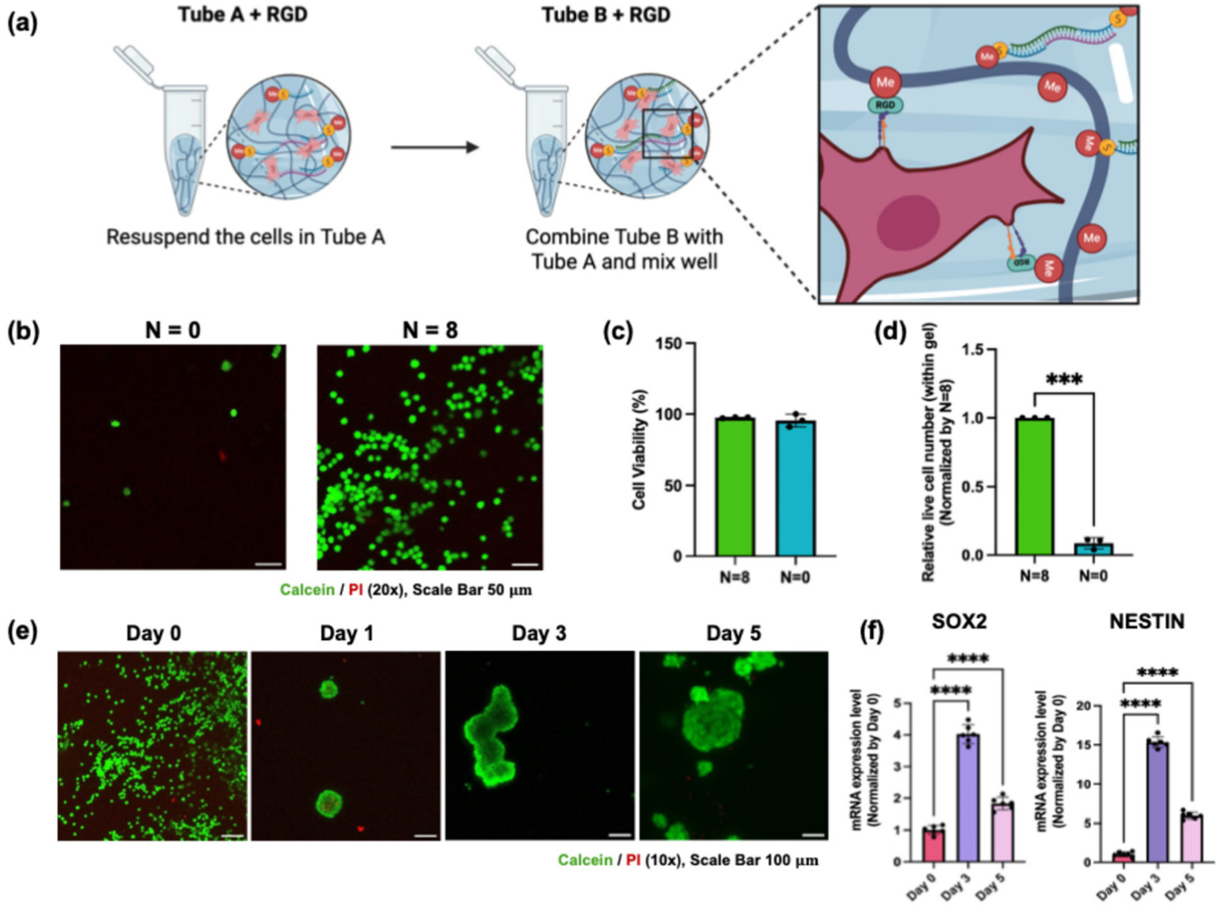

Fig. 5 Encapsulation of neural progenitor cells in the HA–DNA hydrogel. (a) Schematic illustration showing the encapsulation of ReN cells with HA–DNA hydrogel. (b) Representative live/dead staining images of encapsulated ReN cells in hydrogels crosslinked with the randomized lengths of $N = 0$ and $N = 8$. Calcein AM (green) and PI (red). Scale bar, 50 μm. (c) Quantitative analysis of cell viability and (d) live cells within gel at day 0, normalized by $N = 8$. (e) Live/dead assay of ReN cells in HA–DNA hydrogel ($N = 8$) over a period of 5 days. Scale bar, 100 μm. (f) Relative mRNA expression levels of neural stem cell markers *SOX2* and *NESTIN* measured by qPCR (normalized by GAPDH). Statistical differences were obtained by one-way ANOVA followed by Welch's *t*-test (c) and Tukey's test (e). $****P < 0.001$, $***P < 0.005$, $**P < 0.01$, $*P < 0.05$. Graphs show means ± SD.

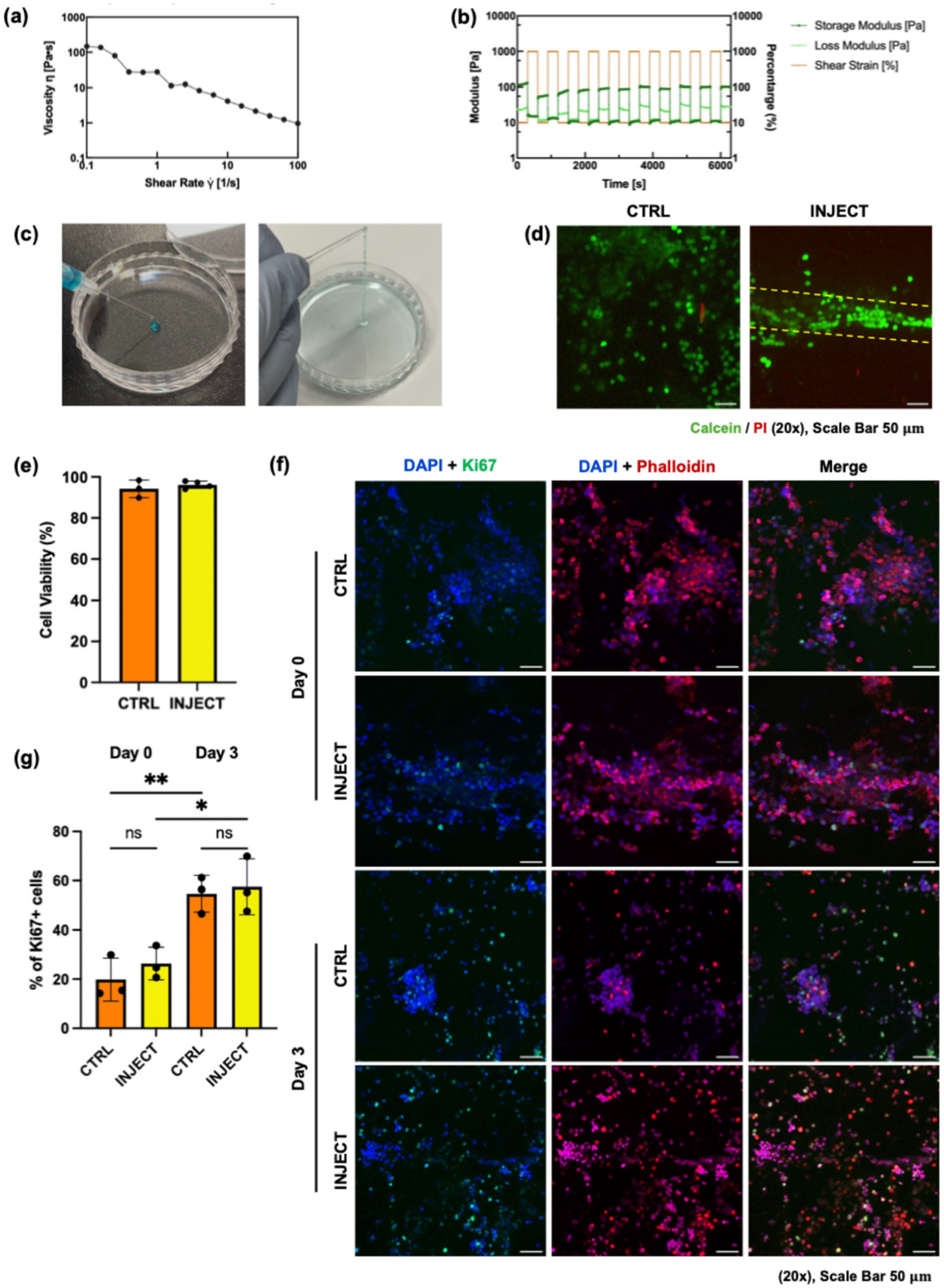

Fig. 6 Injectability of the HA–DNA hydrogel (N = 8). (a) Shear-thinning behavior of the HA–DNA hydrogel. (b) Self-healing test under alternating 1000% (break) strain and 10% (recovery) strain cycle. (c) Images of HA–DNA hydrogel extrusion by syringe of 23-gauge (left) and the hydrogel immersed in PBS after extrusion (right). (d) Confocal stacked image of the live/dead staining of ReN cells encapsulated in CTRL and INJECT hydrogels. Scale bar, 50 μm. (e) Quantitative analysis of the cell viability within CTRL and INJECT conditions with n = 3 biological replicates. (f) Immunofluorescence image of ReN cells stained for Ki-67 (green), phalloidin (red), and DAPI (blue) under CTRL and INJECT conditions at day 0 and day 3. (g) Quantification of Ki-67-positive cells. n = 3 biological replicates. One-way ANOVA followed by Tukey's test (g). ****$P < 0.001$, ***$P < 0.005$, **$P < 0.01$, *$P < 0.05$. Graphs show means ± SD.

permits extrusion without compromising structural integrity after injection.[41] Furthermore, we performed a self-healing test using oscillatory rheology (Fig. 6b). When the HA–DNA hydrogel was subjected to a high strain of 1000%, the material transitioned to a solution-like state ($G'' > G'$). Upon decreasing the strain to 10%, the gel rapidly recovered its storage modulus, exhibiting a restored gel-like behavior ($G' > G''$). Over the course of 10 consecutive breakage–recovery cycles, HA–DNA hydrogel restored more than 90% of its stiffness, demonstrating that the reversible dual-crosslinker system with the randomized domain length of $N = 8$ enables rapid recovery after deformation. This high degree of stiffness recovery implies that the hydrogel can withstand the mechanical disruption imposed during syringe extrusion and rapidly re-establish its network structure after injection, which is essential for maintaining shape fidelity and cell retention. These two results demonstrate that the HA–DNA hydrogel possesses the rheological characteristics essential for injectability and printability.

Based on these results, we further evaluated whether the hydrogel could maintain its structural integrity under realistic syringe injection conditions. HA–DNA hydrogel was extruded through a 23-gauge syringe and incubated at 37 °C for 1 hour. After incubation, the extruded gel was immersed in PBS to assess its post-injection stability (Fig. 6c). During extrusion, the HA–DNA hydrogel exhibited a fluid-like behavior that allowed smooth passage through the syringe. However, after incubation, the gel rapidly regained and maintained a coherent gel structure in PBS, demonstrating that its structural integrity was preserved after extrusion.

We next evaluated cell viability within this gel after injection by comparing injected (INJECT) and non-injected (loaded as a droplet with pipette; CTRL) gels (Fig. 6d). As a result, ReN cells embedded in the gels showed viability above 90% in both CTRL and INJECT gels, indicating that the HA–DNA gel does not significantly compromise cell viability during injection (Fig. 6e). Furthermore, the encapsulated cells aligned along the thread-like HA–DNA hydrogel after injection, demonstrating the preservation of injection-induced morphology. Importantly, early spheroid formation was also comparable between CTRL and INJECT conditions at day 1 using the same initial cell density (Fig. S5), indicating that syringe extrusion does not impair subsequent multicellular aggregation.

We also assessed the proliferative activity of encapsulated cells by staining for Ki-67 (green), a proliferative marker, under two different conditions: within CTRL and INJECT gels (Fig. 6f). At day 0, cells in both CTRL and INJECT hydrogels exhibited limited Ki-67 expression, indicating that most cells remained in a resting (non-proliferative) state. On the other hand, by day 3, the proportion of Ki-67 positive cells increased substantially in both conditions, demonstrating active proliferation within the HA–DNA hydrogel (Fig. 6g). Additionally, the injected condition showed a comparable proliferation level to the CTRL, non-injected control, confirming that the injection process did not impair proliferative capacity.

Taken together, these results clearly suggest that our HA–DNA hydrogel system offers excellent injectability, providing a mechanically resilient and biologically supportive 3D matrix that preserves cell viability and proliferation even after the injection process.

Discussion

In this study, we demonstrate that introducing sequence-level randomness into DNA crosslinkers provides a powerful means to regulate hybridization kinetics and prevent premature network formation that has long hindered the practical use of DNA-based hydrogels. Rather than relying solely on thermodynamic tuning through length or GC-content, our findings highlight the importance of controlling sequence entropy to modulate undesired intramolecular and intermolecular assemblies within concentrated precursor solutions.

A particularly notable insight from our work is that an intermediate level of randomness ($N = 8$) produces a unique balance between suppressing spontaneous hybridization and preserving efficient post-mixing gelation. This suggests that DNA hydrogels operate within a kinetic window, where sequence diversity is sufficient to disrupt nonproductive self-folding yet not so excessive as to introduce new stochastic complementary motifs. Interestingly, when the random domain was excessively extended ($N = 10$) within the overlap domain (14 nt), fortuitous complementary motifs re-emerged, increasing the probability of self-assembly and causing a partial return of pre-gelation. This behavior also reflects a well-known property of DNA hybridization that even a single sequence-level modification can significantly alter the dynamic folding landscape and 3D assembly behavior.[42]

The translational implications of this sequence-level control are significant. The ability to maintain precursor solutions in a stable, low-viscosity state enables reliable syringe delivery and facilitates encapsulation of delicate cell types, such as neural progenitor cells. The optimized $N = 8$ hydrogel maintained excellent biological performance, including stable cell viability, proliferation, and the expression level of key stemness markers even after syringe injection. These findings indicated that our engineered hydrogel not only overcomes uncontrolled gelation kinetics but also establishes a programmable, injectable, and biologically supportive hydrogel platform suitable for neural stem cell delivery and broader tissue-engineering applications. This programmable control over gelation could be broadly advantageous for minimally invasive tissue repair, injectable cell therapies, or *in situ*-forming constructs requiring precise temporal activation.

Nevertheless, one remaining limitation of our system is the inherently high DNA-content requirement, a constraint common to many DNA-based hydrogels.[17] Reducing this burden represents an important direction for broadening clinical feasibility.

Overall, our findings establish sequence randomness as a tunable molecular design parameter for overcoming uncontrolled gelation kinetics, offering a new framework for engineering DNA-hydrogel systems that are both predictable and biologically compatible.

Experimental section

Cell culture

The human neural progenitor cell line ReNcell VM was purchased from Merck (Sigma-Aldrich, SCC008). The cells were cultured on dishes pre-coated with laminin (ThermoFisher, 23017015) at a concentration of 15 μg mL^{-1}. The culture medium was composed of Dulbecco's modified Eagle's medium/nutrient mixture F-12 (DMEM/F12, ThermoFisher, Invitrogen, 11330-032) supplemented with 1× B27 (ThermoFisher, 17504044), 1% penicillin–streptomycin (10 000 U mL^{-1}; ThermoFisher, Gibco, 15140122), basic fibroblast growth factor (bFGF) (20 ng mL^{-1}, Sino Biological), epidermal growth factor (EGF) (20 ng mL^{-1}, Sino Biological), and heparin (2 μg mL^{-1}, Merck, H3149-10KU). For subculturing, the cells were harvested using Accutase (Merck, SCR005). NSCs were incubated in a humidified environment with 5% CO_2 at a constant temperature of 37 °C.

Synthesis of methacrylated hyaluronic acid

Sodium hyaluronate, 1.55 MDa (LIFECORE, HA15M-1), was dissolved to a concentration of 10 mg mL^{-1} in DI water. Methacrylic anhydride (Sigma-Aldrich, 276685) was added dropwise (2–2.25 mL) to continuously adjust pH to 8 with 10 N NaOH (100 μL) while stirring the solution at 4 °C for approximately 6 h. The pH was raised to 10, and the mixture was allowed to react overnight at 4 °C. Subsequently, an additional 0.5 mL of methacrylic anhydride was added, and the pH was maintained between 8 and 9 with NaOH, for a further 4 h at 4 °C. The reaction mixture was readjusted to pH 10 and kept overnight at 4 °C. After the methacrylic anhydride was completely added, the pH was adjusted to approximately 9. The HA-ME solution was precipitated in chilled ethanol (200–250 mL). The precipitate was collected by centrifugation (4000*g*, 15 min, 4 °C), redissolved in DNase-free distilled water to yield a clear HA-ME solution, frozen at −80 °C for 2–3 h, and lyophilized for 3–5 days to obtain the dry HA-ME powder for long-term storage. The degree of methacrylation (DoM) was determined by ^{1}H NMR spectroscopy using the following equation:

$$\mathrm{DoM} = \frac{(I_{5.5\,\mathrm{ppm}} + I_{5.2\,\mathrm{ppm}})/2}{I_{1.9\,\mathrm{ppm}}/3},$$

where $I_{5.5\ \mathrm{ppm}}$ and $I_{5.2\ \mathrm{ppm}}$ correspond to the integrals of the methacrylate vinyl protons, and $I_{1.9\ \mathrm{ppm}}$ represents the integral of the HA *N*-acetyl methyl peak. The calculated DoM value was 0.667.[43,44]

Characterization of HA-ME by ^{1}H-NMR

HA-ME was characterized using ^{1}H-NMR (500 MHz, NM-ECZ500R Console, JEOL, Japan) in deuterium oxide (D_2O). The degree of methacrylation (DoM) of hyaluronic acid was calculated.

Conjugation of the anchor strand to HA-ME

5′-Thiol-modified anchor strand was reduced using 1 N dithiothreitol (DTT) at a volume ratio of 1 : 5 (DTT : anchor strand) to conjugate the free thiol groups with methacrylate groups of HA-ME *via* a thiol–Michael addition reaction. The reduction was allowed to proceed for 15 min at room temperature. Following the incubation, ethyl acetate was added to remove excess DTT, and the phases were separated. The reduced oligonucleotide was collected from the lower aqueous phase. The volume ratio of diluted anchor strand : DTT : ethyl acetate is 5 : 1 : 5. The reduction procedure was carried out according to the manufacturer's protocol (Bioneer, Korea) with minor modifications.

Ellman's assay

The generation of free thiol groups was confirmed using Ellman's assay (DTNB). To ensure experimental accuracy, a cysteine-containing peptide was used as a positive control, whereas no thiol oligonucleotide served as a negative control. Reaction buffer was prepared with 0.1 M sodium phosphate buffer (pH 8.0) containing 1 mM EDTA. DTNB (4 mg) was dissolved in 1 mL of the reaction buffer. The reaction buffer, Ellman's reagent solution, and sample were mixed at a volume ratio of 50 : 1 : 5 and incubated for 15 min at room temperature for color development. The absorbance of the reaction mixture was measured at 412 nm using a microplate reader (DeNovix DS-11, USA).

Agarose gel electrophoresis

Agarose gel electrophoresis was performed to confirm DNA anchor–HA conjugation efficiency and to analyze unbound DNA strands. Agarose gels (1% w/v) were prepared by dissolving agarose powder in 1× TAE buffer (50–100 mL depending on gel size). The mixture was heated in a microwave until fully transparent and allowed to cool slightly before adding gel staining buffer (5 μL per 100 mL). The molten agarose was poured into a gel casting tray fitted with a comb and allowed to solidify for ∼30 min at room temperature. After polymerization, the gel was placed into an electrophoresis chamber and submerged in 0.5× TAE buffer. DNA samples were mixed with 6× loading dye (sample : dye = 5 : 1) unless dye was already included, and a DNA size marker (7 μL) was loaded in the first lane. Electrophoresis was run for 25–30 min to prevent the DNA from migrating out of the gel. Gels were imaged after electrophoresis using a standard gel documentation system.

Thermal annealing of DNA-crosslinked acellular hydrogel

For acellular hydrogels, the samples were prepared at the final concentration of 1% (w/v) HA-ME solution supplemented with 22.8 μM anchor strand, 1150 μM (12.27 g L^{-1}) crosslinker A and B in one tube. The samples were annealed on the thermal cycler using the following steps: (1) heating at 95 °C for 3 min (2) instant cooling from 95 °C to 80 °C, (3) holding at 80 °C for 2 min, (4) first cooling ramp from 80 °C to 65 °C at −0.3 °C min^{-1}, (5) second cooling ramp from 65 °C to 37 °C at −0.5 °C min^{-1}, (6) holding at 37 °C for 1 hour. The first cooling ramp facilitates the binding between the anchor strand and adaptor domain of crosslinker, while the second ramp allows the binding between crosslinker A and crosslinker B. For cellular hydrogels, the thermal annealing process was performed in two separate tubes under the same conditions as described for the acellular hydrogels. Tube A contained the 1% (w/v) HA-ME solution and reduced anchor strand (22.8 μM) with crosslinker A, while Tube B contained the same components except that crosslinker A was replaced with crosslinker B. The process of anchor strand reduction was performed in the same manner as described above. The prepared samples were annealed on the thermal cycler using the following steps: (1) heating at 95 °C for 3 min, (2) cooling from 95 °C to 37 °C at a rate of -3 °C min^{-1}. The cooling ramp promotes hybridization between the anchor strand and the adaptor domain of crosslinker A or B. After the thermal annealing process, the two precursors were maintained at 37 °C.

Oscillatory rheological measurements

The rheological properties of random–sequence-driven DNA crosslinked HA-ME were analyzed using an Anton Paar MCR 302e rheometer (Anton Paar, Austria) with a parallel plate geometry (PP08) and a 0.2 mm gap distance at 37 °C. A thin layer of oil was applied around the edge to prevent evaporation of the hydrogel during measurement. For acellular hydrogels, samples were measured at 37 °C. The time test was performed for 40 min at a strain of 0.5% and an angular frequency of 6 rad s^{-1} to evaluate whether the sample exhibited gel-like or sol-like behavior. Also, the frequency sweep test was performed from 0.1 rad s^{-1} to 10 rad s^{-1} angular frequency at 0.5% strain.

For cellular hydrogels, after the thermal annealing process, an integrin-binding peptide (Anaspec, AS-62349, Ac-GCGYGRGDSPG-NH) was added to each tube to a final concentration of 1 mg mL^{-1}. The samples were then incubated at 37 °C for 2 hours on a shaker to allow the RGD conjugation reaction. After incubation, the two solutions were mixed at room temperature to obtain the DNA crosslinked cellular hydrogel. Rheological time test (0.5%, 6 rad s^{-1}.) and a frequency sweep test (0.1 rad s^{-1}–10 rad s^{-1}, 0.5%) were conducted under identical conditions as described for the acellular hydrogel. To assess the self-healing ability of the cellular hydrogel, the strain was alternated between 1000% and 10% for 5 min per cycle, repeated 10 times at an angular frequency of 6 rad s^{-1}.

NSCs encapsulation in HA–DNA hydrogel

For NSC culture, two precursors were prepared at a final concentration of 1% (w/v) HA-ME with: (a) 22.5 μM reduced anchor strand and 1150 μM (12.27 g L^{-1}) crosslinker A ($N = 8$), (b) 22.5 μM reduced anchor strand and 1150 μM (12.27 g L^{-1}) crosslinker B ($N = 8$). The preparation of tubes (a) and (b) followed the same procedure as described for the cellular thermal annealing process. After the RGD conjugation reaction for 2 hours in each tube, the cell suspension was sequentially mixed with tube (a) and then tube (b) under gentle stirring, at a density of 1 × 10^{6} cells per hydrogel (40 μL). The cell-laden hydrogel was loaded into a confocal dish (Confocal dish Clear Glass 13∅ Hole, SPL, 100350) and then incubated at 37 °C for 1 hour to allow gelation. After gelation, DMEM/F12 medium (1× B27 supplement, 1% penicillin–streptomycin) containing EGF (20 ng mL^{-1}), bFGF (20 ng mL^{-1}), and heparin (2 μg mL^{-1}) was added, and the cell-laden hydrogel was cultured under standard conditions (37 °C, 5% CO_2). The viability of NSCs at certain time points (day 0, day 1, day 3) was evaluated by live/dead assay.

Gene expression analysis

ReN cells were retrieved from the HA–DNA hydrogel at day 0, 3, and 5 using hyaluronidase (10 mg mL^{-1}, Merck, H3884) in DMEM for 1 h at 37 °C. Total RNA was extracted from the cell pellet using the NucleoSpin RNA Plus Mini Kit (MACHEREY-NAGEL, MN740984.50) according to the manufacturer's instructions. The isolated RNA was quantified by Nanodrop spectrophotometry (DeNovix DS-11, USA), and 150 ng of total RNA was reverse-transcribed into cDNA using the ReverTra Ace qPCR RT Master Mix with gDNA Remover (TOYOBO, TOFSQ-301). For quantitative PCR (qPCR), 10 μL of THUNDERBIRD Next SYBR qPCR Mix (TOYOBO, TOQPX-201) was mixed with 1 μL forward primer and reverse primer (10 μM), 5.53 μL cDNA template (100 ng mL^{-1}), and the necessary nuclease-free water to reach a 20 μl final volume reaction per well. Primer sequences are listed in Table 1. Quantitative PCR was performed using the CFX Duet Real-Time PCR System (Bio-Rad, Hercules, California, United States). Relative gene expression was calculated using the $2^{-\Delta\Delta Ct}$ method with GAPDH used as the internal control.

Fluorescence live/dead assay

Cell viability within the HA–DNA hydrogel was evaluated using a live/dead assay. NSCs were stained with 1.5 μM Calcein-AM (ThermoFisher, C3099) and 4.5 μM propidium iodide (Invitrogen, P1304MP) in serum-free medium for 30 min at 37 °C. The samples were washed three times with PBS and then incubated for an additional 5 min in DMEM/F12 medium in a confocal dish. Confocal images were taken on an LSM880 Airyscan confocal microscope (Zeiss) at 10× and 20× magnification.

Immunofluorescence staining of Ki-67

For immunostaining, encapsulated cells were fixed with 4% paraformaldehyde (PFA) (BIOSESANG, PC2205-100-74) for

Table 1 List of primers used

Gene name	Forward primer (5′ to 3′)	Reverse primer (5′ to 3′)
GAPDH	GTCTCCTCTGACTTCAACAGCG	ACCACCCTGTTGCTGTAGCCAA
Nestin	TCAAGATGTCCCTCAGCCTGGA	AAGCTGAGGGAAGTCTTGGAGC
Sox2	GCTACAGCATGATGCAGGACCA	TCTGCGAGCTGGTCATGGAGTT

10 min and permeabilized with 0.3% Triton X-100 and 3% bovine serum albumin (BSA) for 40 min at room temperature. Then, samples were incubated at 4 °C for 3 days with the primary antibody against Ki-67 (1 : 250, Abcam, ab16667). Following PBS washing, samples were treated with donkey anti-rabbit immunoglobulin (IgG) Alexa Fluor 488 (1 : 500, Abcam, ab150073). Counterstaining of the cell nuclei was conducted with 4′,6-diamidino-2-phenylindole (DAPI, Sigma-Aldrich). Additionally, actin filaments were stained using phalloidin conjugated to Alexa Fluor 546 (1 : 3200, Invitrogen, A22283). Samples were incubated overnight at 4 °C. Fluorescence images were acquired using a LSM880 Airyscan confocal microscope (Zeiss) at 10× and 20× magnification.

Statistical analysis

All the quantitative data were presented as the means ± SD. Statistical comparisons were conducted using an independent sample *t*-test or one-way analysis of variance (ANOVA), with the Tukey's test used to make pairwise comparisons between multiple groups.

Thermodynamic analysis using Nupack

To evaluate the intrinsic binding and folding properties of crosslinker sequences, thermodynamic calculations were performed using NUPACK based on minimum free energy (MFE) structure predictions. All simulations were conducted at 37 °C using the DNA nearest-neighbor model.

Tube ensemble analysis

The program sequentially replaces the ambiguous bases N with nucleobases (A, C, G, T) *via* multilayer nested loops. This creates a library of crosslinker A and B variants. The model parameters were set to $T = 37$ °C, 22.8 μM for anchor strand, 1150 μM for crosslinker libraries, and a complex size of 4. For each sequence variant, tube ensemble analysis was performed to compute equilibrium complex concentrations and corresponding minimum free energy (MFE) structures. The equilibrium molar concentrations of desired assembly (anc – crosslinker A or B) and undesired assemblies (anc – anc and identical crosslinker – crosslinker) were extracted and compared across sequence conditions.

Intermolecular self-dimerization analysis

Standard-state free energies ($\Delta G°$) for self-dimerization were calculated for $N = 8$ and $N = 10$ conditions. The number of possible sequence variants scales as 4^n variants (n = the number of N), and the total number of possible pairwise strand interactions scales approximately as $(4^n \times 4^n)/2$. Because exhaustive evaluation of all possible strand pairs is computationally infeasible, 100 000 strand pairs were randomly sampled for each N condition. For each sampled pair, a dimer complex was constructed and its free energy was calculated to quantify intermolecular binding propensity. The mean value across all sampled pairs was used to represent the overall self-dimerization tendency for each N condition.

Author contributions

T. K., E. H., and J. B. designed research; T. K. and E. H. performed research; T. K., E. H., S. P., and J. B. contributed new reagents/analytic tools; T. K., E. H., and J. B. analyzed data; and T. K., E. H., and J. B. wrote the paper.

Conflicts of interest

The authors declare that they have no competing financial interests.

Data availability

This manuscript reports original experimental data generated and analysed as part of this study.

Supplementary information (SI) is available. See DOI: https://doi.org/10.1039/d5nr05011a.

Acknowledgements

This work was supported by the National Research Foundation of Korea (NRF) grants funded by the Korea government (MSIT) (No. RS-2023-00213047 and RS-2024-00405818).

References

1 J. Lam, N. F. Truong and T. Segura, *Acta Biomater.*, 2014, **10**, 1571–1580.
2 B. Cai, J. Fang, S. Zhou, M. Xie, K. Zhang, J. Li and G. Yin, *Int. J. Biol. Macromol.*, 2025, **295**, 139566.
3 J. A. Burdick and G. D. Prestwich, *Adv. Mater.*, 2011, **23**, H41–H56.
4 H. Yu, J. Zhang, L. Yang, Y. Tian, C. Milne, P. Jin, Q. Li, R. Song and W. Wang, *J. Controlled Release*, 2025, **385**, 113985.
5 S. H. Park, J. Y. Seo, J. Y. Park, Y. B. Ji, K. Kim, H. S. Choi, S. Choi, J. H. Kim, B. H. Min and M. S. Kim, *NPG Asia Mater.*, 2019, **11**, 30.
6 J. Baek, P. A. Lopez, S. Lee, T. S. Kim, S. Kumar and D. V. Schaffer, *Sci. Adv.*, 2022, **8**, eabm4646.
7 J. Baek, S. Kumar, D. V. Schaffer and S. G. Im, *Biomater. Sci.*, 2022, **10**, 6768–6777.
8 Y. Deng, J. Ren, G. Chen, G. Li, X. Wu, G. Wang, G. Gu and J. Li, *Sci. Rep.*, 2017, **7**, 2699.
9 G. Demirel, Y. D. Cakıl, G. Koltuk, R. G. Aktas and M. Calıskan, *Sci. Rep.*, 2024, **14**, 19560.
10 Z. Wang, R. Chen, S. Yang, S. Li and Z. Gao, *Mater. Today Bio*, 2022, **16**, 100430.
11 A. Orr, P. Wilson and T. Stotesbury, *ACS Appl. Polym. Mater.*, 2023, **5**, 583–592.

12 R. Shi, K.-L. Chen, J. Fern, S. Deng, Y. Liu, D. Scalise, Q. Huang, N. J. Cowan, D. H. Gracias and R. Schulman, *Nat. Commun.*, 2024, **15**, 7773.

13 W. Yu, E. Gong, C. Wang, C. Che, Y. Zhao, X. Wu, Y. Yang, H. Shi, M. Chen, M. Li, L. Xie, Y. Guo, M. Guo, L. Mu, Z. Wang, Z. Zhang, K. Zhang, J. Liu and J. Shi, *Sci. Adv.*, 2024, **10**, eado3919.

14 M. Chen, Y. Wang, J. Zhang, Y. Peng, S. Li, D. Han, S. Ren, K. Qin, S. Li and Z. Gao, *J. Nanobiotechnol.*, 2022, **20**, 40.

15 S. Lu, S. Wang, J. Zhao, J. Sun and X. Yang, *Chem. Commun.*, 2018, **54**, 4621–4624.

16 H. Cao, L. Duan, Y. Zhang, J. Cao and K. Zhang, *Signal Transduction Targeted Ther.*, 2021, **6**, 426.

17 R. Wu, W. Li, P. Yang, N. Shen, A. Yang, X. Liu, Y. Ju, L. Lei and B. Fang, *J. Nanobiotechnol.*, 2024, **22**, 518.

18 R. Shi, H. Zhan, S. Jiang, K. Lin and C. Yuan, *Adv. Sci.*, 2025, **12**, e11099.

19 S. Fujita, S. Hara, A. Hosono, S. Sugihara, H. Uematsu and S.-i. Suye, *Adv. Polym. Technol.*, 2020, **2020**, 1470819.

20 R. Acharya, S. D. Dutta, H. Mallik, T. V. Patil, K. Ganguly, A. Randhawa, H. Kim, J. Lee, H. Park, C. Mo and K.-T. Lim, *J. Nanobiotechnol.*, 2025, **23**, 233.

21 P. Bertsch, M. Diba, D. J. Mooney and S. C. G. Leeuwenburgh, *Chem. Rev.*, 2023, **123**, 834–873.

22 S. Maity, K. Mahata, B. Meshram and S. Banerjee, *ACS Polym. Au*, 2025, **5**(6), 680–711.

23 F. Cancilla, A. Martorana, C. Fiorica, G. Pitarresi, E. F. Craparo, S. E. Drago and F. S. Palumbo, *Int. J. Pharm.*, 2025, **685**, 126233.

24 H. Wang, H. Wang, H. Pian, F. Su, F. Tang, D. Chen, J. Chen, Y. Wen, X. C. Le and Z. Li, *Anal. Chem.*, 2024, **96**, 12022–12029.

25 Y. Zhang, L. Zhu, J. Tian, L. Zhu, X. Ma, X. He, K. Huang, F. Ren and W. Xu, *Adv. Sci.*, 2021, **8**, 2100216.

26 Y.-H. Peng, S.-K. Hsiao, K. Gupta, A. Ruland, G. K. Auernhammer, M. F. Maitz, S. Boye, J. Lattner, C. Gerri, A. Honigmann, C. Werner and E. Krieg, *Nat. Nanotechnol.*, 2023, **18**, 1463–1473.

27 Z. Luo, Y. Wang, Y. Xu, J. Wang and Y. Yu, *Smart Med.*, 2023, **2**, e20230029.

28 J. B. Leach and C. E. Schmidt, *Biomaterials*, 2005, **26**, 125–135.

29 M. H. M. Oudshoorn, R. Rissmann, J. A. Bouwstra and W. E. Hennink, *Polymer*, 2007, **48**, 1915–1920.

30 F. Huang, M. Chen, Z. Zhou, R. Duan, F. Xia and I. Willner, *Nat. Commun.*, 2021, **12**, 2364.

31 S. A. Ferreira, M. S. Motwani, P. A. Faull, A. J. Seymour, T. T. L. Yu, M. Enayati, D. K. Taheem, C. Salzlechner, T. Haghighi, E. M. Kania, O. P. Oommen, T. Ahmed, S. Loaiza, K. Parzych, F. Dazzi, O. P. Varghese, F. Festy, A. E. Grigoriadis, H. W. Auner, A. P. Snijders, L. Bozec and E. Gentleman, *Nat. Commun.*, 2018, **9**, 4049.

32 D. Zauchner, M. Z. Müller, M. Horrer, L. Bissig, F. Zhao, P. Fisch, S. S. Lee, M. Zenobi-Wong, R. Müller and X.-H. Qin, *Nat. Commun.*, 2024, **15**, 5027.

33 G. L. Ellman, *Arch. Biochem. Biophys.*, 1959, **82**, 70–77.

34 P. Moshayedi, L. R. Nih, I. L. Llorente, A. R. Berg, J. Cinkornpumin, W. E. Lowry, T. Segura and S. T. Carmichael, *Biomaterials*, 2016, **105**, 145–155.

35 G. Sicilia, C. Grainger-Boultby, N. Francini, J. P. Magnusson, A. O. Saeed, F. Fernández-Trillo, S. G. Spain and C. Alexander, *Biomater. Sci.*, 2014, **2**, 203–211.

36 A. J. Simon, L. T. Walls-Smith and K. W. Plaxco, *Analyst*, 2018, **143**, 2531–2538.

37 M. Glaser, P. Mollenkopf, D. Prascevic, C. Ferraz, J. A. Käs, J. Schnauß and D. M. Smith, *Nanoscale*, 2023, **15**, 7374–7383.

38 J.-T. Kim, S. M. Cho, D. H. Youn, E. P. Hong, C. H. Park, Y. Lee, H. Jung and J. P. Jeon, *Acta Biomater.*, 2023, **167**, 335–347.

39 J. Ahlfeld, S. Filser, F. Schmidt, A. K. Wefers, D. J. Merk, R. Glaß, J. Herms and U. Schüller, *Sci. Rep.*, 2017, **7**, 6137.

40 M. S. Huang, B. L. LeSavage, S. Ghorbani, A. E. Gilchrist, J. G. Roth, C. Huerta-López, E. A. Mozipo, R. S. Navarro and S. C. Heilshorn, *Nat. Commun.*, 2025, **16**, 5213.

41 M. H. Chen, L. L. Wang, J. J. Chung, Y.-H. Kim, P. Atluri and J. A. Burdick, *ACS Biomater. Sci. Eng.*, 2017, **3**, 3146–3160.

42 J. X. Zhang, J. Z. Fang, W. Duan, L. R. Wu, A. W. Zhang, N. Dalchau, B. Yordanov, R. Petersen, A. Phillips and D. Y. Zhang, *Nat. Chem.*, 2018, **10**, 91–98.

43 M. Pérez-Lloret and A. Erxleben, *ACS Omega*, 2024, **9**, 25914–25921.

44 S. A. Bencherif, A. Srinivasan, F. Horkay, J. O. Hollinger, K. Matyjaszewski and N. R. Washburn, *Biomaterials*, 2008, **29**, 1739–1749.